Earth and Planetary Science Letters 414 (2015) 68–76

Contents lists available at ScienceDirect

Earth and Planetary Science Letters

www.elsevier.com/locate/epsl

Lower mantle superplume growth excites geomagnetic reversals

Hagay Amit [a,*], Peter Olson [b]

[a] CNRS UMR 6112, Université de Nantes, Laboratoire de Planétologie et de Géodynamique, 2 rue de la Houssinière, Nantes, F-44000, France
[b] Department of Earth and Planetary Sciences, Johns Hopkins University, Baltimore, MD 21218, USA

ARTICLE INFO

Article history:
Received 1 September 2014
Received in revised form 5 January 2015
Accepted 11 January 2015
Available online xxxx
Editor: Y. Ricard

Keywords:
geodynamo
polarity reversals
core convection
core–mantle boundary
D″ layer
superplumes

ABSTRACT

Seismic images of the lower mantle reveal two large-scale, low shear wave velocity provinces beneath Africa and the Pacific that are variously interpreted as superplumes, plume clusters or piles of dense mantle material associated with the D″ layer. Here we show that time variations in the height of these structures produce variations in heat flux across the core–mantle boundary that can control the rate at which geomagnetic polarity reversals occur. Superplume growth increases the mean core–mantle boundary heat flux and its lateral heterogeneity, thereby stimulating polarity reversals, whereas superplume collapse decreases the mean core–mantle boundary heat flux and its lateral heterogeneity, inhibiting polarity reversals. Our results suggest that the long, stable polarity geomagnetic superchrons such as occurred in the Cretaceous, Permian, and earlier in the geologic record were initiated and terminated by the collapse and growth of lower mantle superplumes, respectively.

1. Introduction

Paleomagnetic data records extreme variability in the rate at which the geomagnetic field has reversed its polarity, from hyper-reversing periods in which the geomagnetic field reversed as often as every 40 thousand years, to superchrons in which the polarity remained stable for 40 million years (e.g. Merrill et al., 1998; Gradstein et al., 2012). There is little doubt that some of this variability is intrinsically random, and arises from the stochastic nature of the dynamo process (Ryan and Sarson, 2007; Wicht et al., 2009). However, the reversal record over the whole of Phanerozoic time is far from random (Olson et al., 2014). Its non-random behavior includes the approximately 200 million years repeat time for superchrons as well as their approximately 40 million years durations (Fig. 1). Both of these far exceed any known timescale of the fluid dynamics intrinsic to the outer core, but they are commensurate with timescales inferred for the variability of mantle dynamics, specifically, the overturn timescale of mantle convection and the development times of deep mantle plumes, respectively. Although mantle dynamics has been widely implicated in controlling geomagnetic reversal frequency (Glatzmaier et al., 1999; Kutzner and Christensen, 2004; Driscoll and Olson, 2009b, 2011; Olson et al., 2010, 2013; Pétrélis et al., 2011; Zhang and Zhong, 2011; Biggin et al., 2012; Olson and Amit, 2014), the precise connection remains enigmatic.

Answers to the puzzle of paleomagnetic reversal variations and their relation to mantle convection history can be found in the structure and dynamical behavior of the D″ layer at the base of the lower mantle. The pattern of seismic heterogeneity in the D″ layer that defines the large low shear velocity provinces (e.g. Garnero and McNamara, 2008), which is dominated in the present-day mantle by a spherical harmonic degree 2 (Dziewonski et al., 2010), has been variously interpreted as the long-lived root structure of two mantle superplumes (Romanowicz and Gung, 2002; Torsvik et al., 2010), plume clusters (Schubert et al., 2004; Bull et al., 2009) or dense chemical piles lying just above the core–mantle boundary (CMB) (Tackley, 2002; McNamara and Zhong, 2005; Tan and Gurnis, 2007). In this paper we make no distinction between these alternatives, using the terms *piles* and *superplumes* interchangeably for the two large seismic structures located in the lowermost mantle beneath Africa and the central Pacific.

How might lower mantle piles influence the long-term behavior of the geodynamo? The most obvious way is by controlling the heat loss from the core, which in turn controls the energy available to drive the geodynamo and its reversals. Models of the general circulation of the mantle (Zhang and Zhong, 2011; Olson et al., 2013) and inferences based on the interpretation of D″ structure (e.g. Masters et al., 2000) indicate that the CMB heat flux below the two piles is lower than the mean for the CMB as a whole, and likewise, the CMB heat flux is higher than the mean in regions where the piles are absent. In mantle general circulation

* Corresponding author.
E-mail address: Hagay.Amit@univ-nantes.fr (H. Amit).

http://dx.doi.org/10.1016/j.epsl.2015.01.013
0012-821X/

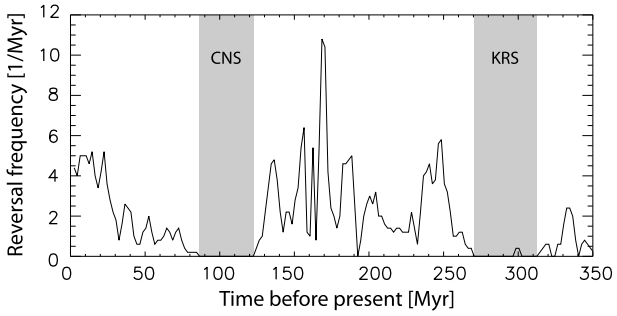

Fig. 1. Average paleomagnetic reversal frequency for 0–350 Ma based on the geomagnetic polarity time scale of Gradstein et al. (2012). The Cretaceous Normal Polarity Superchron (CNS) and Kiaman Reverse Polarity Superchron (KRS) are shaded. The bin size is 5 Myrs and the bin step is 2 Myrs.

models, this variation is a consequence of the flow pattern, which advects dense D″ material into piles beneath upwellings, reducing core heat flux there, and advects dense D″ material from beneath downwellings, increasing the core heat flux at those locations.

If the locations of the two main piles have remained relatively fixed (Burke et al., 2008; Dziewonski et al., 2010; Burke, 2011), the heat flux from the core could still have fluctuated if the heights of the piles changed with time. Figs. 2a and b illustrate how time variability in core heat flux might be produced this way. In the fully collapsed state the dense D″ layer has uniform thickness, and assuming the heat flux across this layer is by conduction, the CMB heat flux is laterally homogeneous. As the piles grow, the increase in the thermal gradient where the D″ layer is thinned exceeds the decrease in the thermal gradient where it is thickened, so that the mean heat flux from the core increases, along with its lateral variation. Assuming that the volume of the D″ layer is conserved and that the temperature difference between the CMB and the top of the D″ layer remains unchanged, growth and collapse of the piles yield large fluctuations in the mean CMB heat flux and its lateral variation, both of which affect the geodynamo and its reversals. Fig. 2c shows that this same argument applies to growth and collapse of a single pile, as has been argued was the case during the assembly of Pangaea (Zhang et al., 2010).

Numerical dynamo simulations show that when the convection in the outer core is stronger the probability for a reversal is larger (Christensen and Aubert, 2006; Olson and Christensen, 2006; Aubert et al., 2009; Driscoll and Olson, 2009b), so that increasing mean CMB heat flux increases reversal frequency (Driscoll and Olson, 2009a, 2011). In numerical dynamos with heterogeneous CMB heat flux patterns, increasing amplitude of boundary heterogeneity usually increases reversal frequency (Kutzner and Christensen, 2004; Olson et al., 2010; Heimpel and Evans, 2013), in particular for the present day tomographic heterogeneity (Olson and Amit, 2014). Another factor that may affect reversal frequency evident in specific zonal patterns is the amount of equatorial vs. polar heat flux (Glatzmaier et al., 1999; Kutzner and Christensen, 2004; Olson et al., 2010), but this effect depends on the dynamo internal control parameters in a non-trivial way. Close to the onset of reversals increased equatorial heat flux may increase reversal frequency, whereas far from the onset increased equatorial heat flux decreases reversal frequency (see geographic vs. inertial controls in Olson and Amit, 2014). Finally, increased equatorial symmetry in the CMB heat flux pattern may stabilize the dipole (Pétrélis et al., 2009, 2011).

Relating the observed variations in the paleomagnetic reversal frequency to the history of the mantle turns out to be a challenging task. Zhang and Zhong (2011) imposed plate tectonics reconstruction as a mechanical boundary condition on mantle convection simulations. Olson et al. (2013) used the time-dependent CMB heat flux model of Zhang and Zhong (2011) as a thermal outer boundary condition on a numerical dynamo simulation in an attempt to reproduce the paleomagnetic reversal frequency. The immediate problem is that during the Cretaceous Normal Superchron (CNS) plates speeds are relatively high (e.g. Lithgow-Bertelloni and Richards, 1998), the corresponding mantle convection vigor and mean CMB heat flux are stronger than average (Zhang and Zhong, 2011), and the predicted core convection and reversal frequency are therefore also higher than usual (Olson et al., 2013), in striking contradiction to the paleomagnetic observation. In contrast, Olson et al. (2013) recovered well the KRS superchron, because in their mantle convection model the D″ piles were (partially) collapsed at that time and the CMB heat flux was weaker than average, behaviors which support our model.

Olson and Amit (2014) demonstrated that reversal frequency varies linearly with a non-dimensional number which they termed the heterogeneity-corrected local Rossby number. This number combines the conventional local Rossby number and the amplitude of the CMB heterogeneity. Although the validity of this linear relation was demonstrated in a rather narrow range of parameter space and it is plausible that it would fail at more realistic conditions these results can be applied qualitatively within the context of a particular set of dynamo parameters. Since it has been shown that it is difficult to explain the variations in reversal frequency by the mean CMB heat flux alone, it could be that the time-dependent amplitude of heterogeneity may help explaining this observation. Finally, possible changes in the CMB heat flux pattern, in particular equatorial vs. polar contributions, should also be considered.

In this paper we develop a simple model of D″ piles that relates the mean CMB heat flux and the amplitude of its lateral heterogeneity to the D″ piles height. We impose the resulting CMB heat

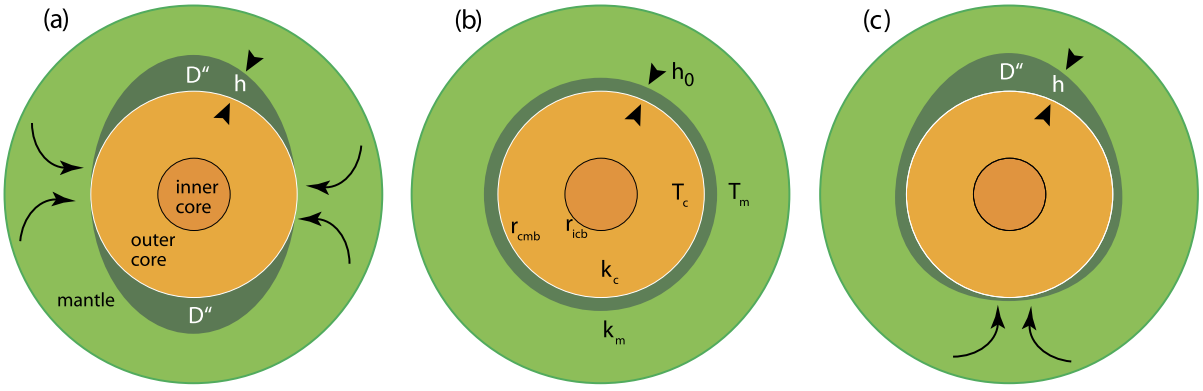

Fig. 2. Schematic illustration of D″ structure. (a) Equatorial section illustrating the dual lower mantle pile configuration with variable height h; (b) Same section illustrating fully collapsed piles configuration, where h_0 is the layer thickness in the collapsed configuration; (c) As in (a) for the single pile configuration. Arrows in (a) and (c) indicate mantle downwellings above regions of thin D″ layer.

Table 1
Non-dimensional mean CMB heat flux q_0^* and heterogeneity amplitude δq^* as functions of non-dimensional piles height amplitude H^* (11). The maximum allowed value H^*_{max} (6) is also given. Expressions are given for the lowest two zonal spherical harmonics planforms. Note that the magnitude of the dual pile planform is different than its conventional value due to (5).

Pile configuration	$f(\phi,\theta)$	q_0^*	δq^*	H^*_{max}
Rotated Y_1^0/single	$\cos\theta$	$\frac{1}{2H^*}\ln\frac{1+H^*}{1-H^*}$	$\frac{H^*}{1-H^{*2}}$	1
Rotated Y_2^0/dual	$\frac{2}{3}(3\cos^2\theta-1)$	$\sqrt{\frac{3}{2H^*(3-2H^*)}}\tan^{-1}(\sqrt{\frac{6H^*}{3-2H^*}})$	$\frac{H^*}{1+\frac{2}{3}H^*-\frac{8}{9}H^{*2}}$	$\frac{3}{2}$

flux as an outer boundary condition on numerical dynamo simulations to establish quantitatively the connection between the height of the D″ piles and the dynamo reversal frequency. We show that lower mantle piles growth can switch the dynamo from non-reversing (superchron) to reversing dynamo states, and conversely, piles collapse can lead to superchron conditions in the core.

2. D″ pile model

Fig. 2 illustrates our D″ pile model in the fully developed and fully collapsed states. The D″ layer thickness h can be generally written as the sum of two parts, a mean thickness h_0 and a spatially varying deviation h':

$$h = h_0 + h' \tag{1}$$

The average of h' over the CMB spherical surface is by definition zero. We conserve the total volume of the D″ layer, i.e., we assume that h_0 is constant with time. The deviation h' is represented as

$$h' = Hf(\phi,\theta) \tag{2}$$

where H is a time-dependent amplitude and $f(\phi,\theta)$ is a planform function representing the spatial heterogeneity, with ϕ and θ being longitude and co-latitude spherical coordinates measured with respect to the symmetry axis of the piles. The amplitude H varies on the long timescale of mantle dynamics (tens of Myr overturn), which is much longer than the overturn time in the core (centuries), so that the core is assumed to be in thermal and magnetohydrodynamical equilibrium with H at every epoch. This separation of timescales between core and mantle overturn times allows us to model the dynamo response at each epoch assuming that H is fixed over that epoch.

If the pile height is non-dimensionalized as $H^* = H/h_0$, the non-dimensional form of (1) becomes

$$h^* = 1 + H^* f(\phi,\theta) \tag{3}$$

The non-dimensional pile height H^* may be generally defined by half the difference between the extremes of h^* (in analogy to the definition of non-dimensional heat flux, e.g. Olson and Christensen, 2002):

$$H^* = \frac{h^*_{max} - h^*_{min}}{2} \tag{4}$$

This constrains the magnitude of the planform function to satisfy

$$\frac{f_{max} - f_{min}}{2} = 1 \tag{5}$$

Finally, to ensure that h^* remains positive over the entire CMB, the pile height is limited by

$$H^* < \frac{1}{|f_{min}|} \equiv H^*_{max} \tag{6}$$

Because the D″ layer is assumed to be in conductive equilibrium with the lower mantle and the outer core, the CMB heat flux obeys Fourier's law:

$$q = k_m \frac{\Delta T}{h} \tag{7}$$

where k_m is lower mantle thermal conductivity and $\Delta T = T_c - T_m$ is the temperature difference across the D″ layer. As in (1), the CMB heat flux is written as the sum of two parts, a mean part q_0 plus a spatially varying heterogeneity q':

$$q = q_0 + q' \tag{8}$$

Combining (1)–(8) gives

$$q_0 + q' = \frac{k_m \Delta T}{h_0 + Hf(\phi,\theta)} \tag{9}$$

Note that both q_0 and q' in (9) are time-dependent. We now define a non-dimensional CMB heat flux $q^* = q/Q$, where $Q = k_m \Delta T/h_0$ corresponds to the CMB heat flux in the fully collapsed pile state (see Fig. 2b). The non-dimensional form of (9) is then

$$q_0^* + q'^* = \frac{1}{1 + H^* f(\phi,\theta)} \tag{10}$$

with the mean non-dimensional heat flux defined as

$$q_0^* = \frac{1}{4\pi}\int_S \frac{1}{1 + H^* f(\phi,\theta)} \sin\theta d\phi d\theta \tag{11}$$

where S denotes a spherical integration. This integral depends on the specific spatial form of $f(\phi,\theta)$; analytical solutions to the lowest two zonal spherical harmonics are given in Table 1 and shown in Fig. 3a. Spherical harmonic Y_1^0 corresponds to the single pile or plume configuration; Y_2^0 corresponds to the dual pile or plume configuration.

The amplitude of the CMB heat flux heterogeneity can be defined in terms of its peak-to-peak difference as (Olson and Christensen, 2002)

$$\delta q = \frac{q_{max} - q_{min}}{2} \tag{12}$$

Normalized by the heat flux scale Q, (12) becomes

$$\delta q^* = \frac{q_{max} - q_{min}}{2Q} \tag{13}$$

Considering the D″ model (10), the non-dimensional amplitude of the CMB heat flux heterogeneity (13) also varies from one pile configuration to another; analytical solutions to the single and dual pile configurations are given in Table 1 and shown in Fig. 3b. Note that as with q_0^* (Fig. 3a), for both configurations the δq^* curves approach infinity as H^* approaches H^*_{max}. Also note the larger q_0^* and δq^* values for the single pile configuration, for a given H^*, compared to the dual pile configuration.

3. Dynamo reversals driven by lower mantle piles

To demonstrate how the growth of lower mantle piles can excite magnetic reversals, we impose the CMB heat flux boundary conditions from the previous section on the outer boundary of low resolution numerical dynamos that include compositional forcing

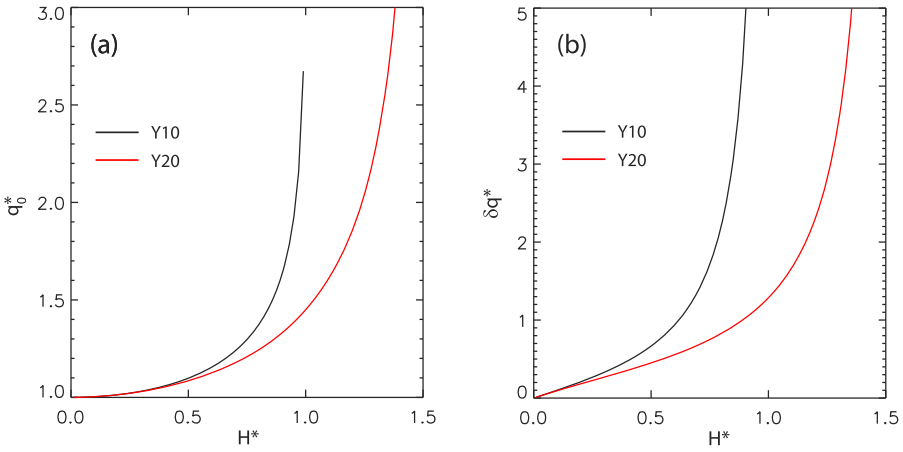

Fig. 3. (a) Non-dimensional mean CMB heat flux q_0^* vs. non-dimensional piles height H^*; (b) Non-dimensional CMB heat flux heterogeneity amplitude δq^* vs. non-dimensional piles height H^*. The curves are based on the analytical solutions given in Table 1. Single pile configurations are in black, dual pile configurations are in red. Both configurations are restricted to the range $H^*_{max} > H^* > 0$ (see (6) and Table 1). (For interpretation of the references to color in this figure legend, the reader is referred to the web version of this article.)

due to inner core growth. We make use of the co-density formulation (Braginsky and Roberts, 1995) in which $C = \rho(\alpha T + \beta\chi)$ where ρ is mean density, T is temperature, χ is the light element concentration (mixing ratio) in the outer core, and α and β are their respective expansivities. For the non-dimensional governing equations see e.g. Christensen and Aubert (2006). Control parameters for these dynamos include the Ekman number E, the Prandtl number Pr and the magnetic Prandtl number Pm defined respectively by

$$E = \frac{\nu}{\Omega D^2}, \qquad Pr = \frac{\nu}{\kappa}, \qquad Pm = \frac{\nu}{\eta} \tag{14}$$

where ν is kinematic viscosity, Ω is the angular velocity of rotation, D is the outer core shell thickness, κ is the diffusivity of the co-density and η is magnetic diffusivity. Buoyancy is parameterized in terms of the Rayleigh number Ra, which can be defined for thermochemical dynamos as (Olson, 2007)

$$Ra = \frac{\beta g D^5 \dot{\chi}}{\kappa \nu^2} \tag{15}$$

where g is gravity at the CMB and $\dot{\chi}$ is the time rate of change of the light element concentration (mixing ratio) in the outer core due to inner core growth. Here we have used D and D^2/ν to scale length and time, respectively, and $\rho\beta D^2\dot{\chi}/\nu$ to scale co-density. The final internal control parameter is ϵ, the sink (or source) term that appears in the co-density transport equation (Christensen and Wicht, 2007), which models the combined effects of the rate of mixing of light elements in the outer core, secular cooling of the outer core, curvature of the core adiabat, and radioactive heat sources; Here we use $\epsilon = -1$, corresponding to a volumetric sink that absorbs all the buoyancy flux that enters the outer core through the inner core boundary, appropriate for convection that is primarily compositionally-driven.

The thermal and compositional boundary conditions for the numerical dynamo models are expressed in terms of the non-dimensional co-density, C^*. At the ICB we set $C^* = 1$, assuming uniform temperature and composition there. At the CMB we impose a heat flux pattern consistent with our piles models. Fig. 4 shows maps of CMB heat flux corresponding to single and dual piles configurations. Fig. 4a shows a map of the CMB heat flux with a pattern of lateral heterogeneity based on the model of lower mantle seismic heterogeneity by Dziewonski et al. (2010). This map has a mean heat flux of $q_0 = 100$ mW/m^2, close to the adiabatic heat flux in the outer core for an assumed thermal

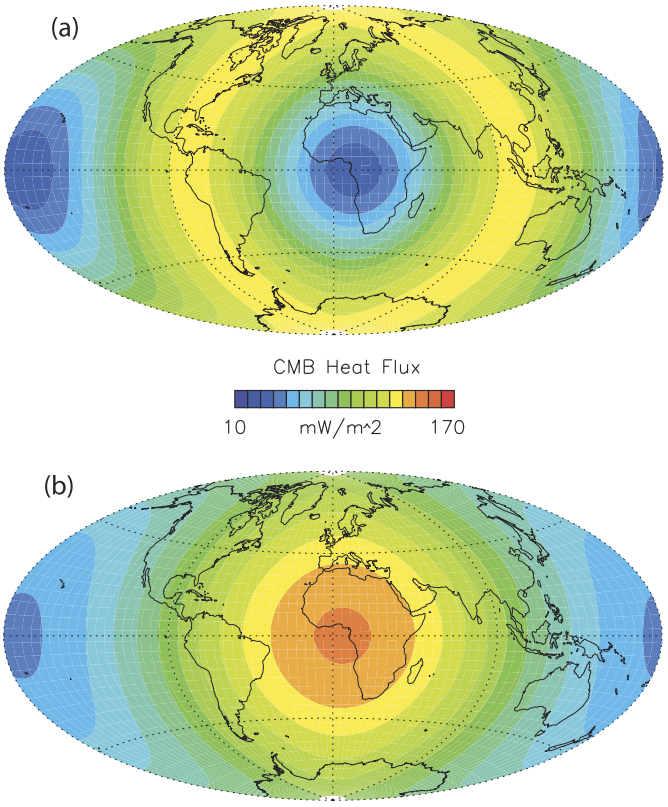

Fig. 4. CMB heat flux patterns in the dual (a) and single (b) superplume configurations. The same 100 mW/m^2 mean heat flux applies to both cases. The peak-to-peak variation is 60 and 100 mW/m^2 in (a) and (b), respectively.

conductivity of $k_c = 130$ W/m/K, and a lateral heterogeneity amplitude of $\delta q = 30$ mW/m^2. Its heterogeneity pattern, which is a close approximation to our dual pile model f, was generated using the following three spherical harmonics measured in longitude and co-latitude coordinates: Y_2^0, Y_2^2 and Y_1^1, with amplitudes in relative proportions of 10 : 10 : 1, respectively. For comparison, Fig. 4b shows a map of the CMB heat flux pattern for a single pile configuration. This map has the same mean heat flux of $q_0 = 100$ mW/m^2 but the heterogeneity amplitude is $\delta q = 50$ mW/m^2.

In order to use CMB heat flux patterns like those shown in Fig. 4 as outer boundary conditions in our numerical dynamo models, two steps are necessary. First, the adiabatic CMB heat flux q_{ad}

Table 2
Dynamo models setup and main results for models with $E = 6 \cdot 10^{-3}$ and dual pile configuration (top), $E = 1 \cdot 10^{-3}$ and dual pile configuration (middle) and $E = 6 \cdot 10^{-3}$ and single pile configuration (bottom). For variables definitions see main text.

H^*	$2\delta q^*$	q_0/Q	q_0 [W/m^2]	q_0/q_{ad}	q^*_{0c}	$\sigma(q^*_{0c})$	Ra	τ_d	Dipole	N	ω_{sh}
10^{-5}	10^{-5}	1	0.05	0.5	−0.03	10^{-7}	$0.6 \cdot 10^5$	16	1.15 ± 0.05	0	na
0.61	0.57	1.13	0.06	0.57	−0.02	0.008	$0.7 \cdot 10^5$	16	1.2 ± 0.1	0	na
0.86	0.94	1.29	0.06	0.65	−0.02	0.01	$0.8 \cdot 10^5$	16	0.9 ± 0.2	0	na
1.0	1.29	1.45	0.07	0.72	−0.01	0.01	$0.9 \cdot 10^5$	80	0.7 ± 0.2	0	na
1.10	1.67	1.61	0.08	0.81	−0.01	0.02	10^5	70	0.65 ± 0.22	0	na
1.18	2.15	1.80	0.09	0.90	−0.003	0.02	$1.1 \cdot 10^5$	225	0.60 ± 0.23	0	na
1.21	2.39	1.89	0.09	0.95	−0.002	0.02	$1.15 \cdot 10^5$	150	0.50 ± 0.24	1	na
1.24	2.69	2.00	0.10	1.0	0	0.02	$1.2 \cdot 10^5$	510	0.43 ± 0.23	21	0.44
1.26	2.94	2.09	0.10	1.04	0.001	0.02	$1.25 \cdot 10^5$	240	0.45 ± 0.24	18	0.34
1.28	3.22	2.18	0.11	1.09	0.002	0.02	$1.3 \cdot 10^5$	220	0.44 ± 0.25	23	0.27
1.30	3.56	2.29	0.11	1.14	0.004	0.02	$1.4 \cdot 10^5$	218	0.47 ± 0.24	25	0.25
1.32	3.98	2.42	0.12	1.21	0.005	0.02	$1.5 \cdot 10^5$	335	0.34 ± 0.26	59	0.24
1.34	4.43	2.60	0.13	1.30	0.007	0.03	$1.6 \cdot 10^5$	310	0.32 ± 0.23	65	0.24
1.18	2.15	1.80	0.09	0.90	−0.003	0.011	$14 \cdot 10^5$	65	1.0 ± 0.13	0	na
1.3	3.56	2.29	0.11	1.14	0.004	−0.013	$18 \cdot 10^5$	65	0.44 ± 0.28	4	0.48
0.705	1.47	1.25	0.06	0.64	−0.02	0.02	$0.75 \cdot 10^5$	80	1.04 ± 0.18	0	na
0.854	3.15	1.49	0.07	0.74	−0.01	0.03	$0.9 \cdot 10^5$	167	0.72 ± 0.18	0	na
0.9175	5.80	1.71	0.09	0.86	−0.005	0.05	$1.0 \cdot 10^5$	165	0.63 ± 0.18	0	na
0.9375	7.74	1.83	0.09	0.92	−0.003	0.06	$1.1 \cdot 10^5$	250	0.30 ± 0.18	20	0.35
0.9575	11.51	2.00	0.10	1.00	$-6 \cdot 10^7$	0.09	$1.2 \cdot 10^5$	250	0.25 ± 0.12	34	0.30
0.97	16.41	2.16	0.11	1.08	0.002	0.11	$1.3 \cdot 10^5$	242	0.16 ± 0.09	44	0.19
0.98	24.75	2.34	0.12	1.17	0.004	0.16	$1.4 \cdot 10^5$	222	0.14 ± 0.08	53	0.17
0.985	33.08	2.48	0.12	1.24	0.006	0.20	$1.5 \cdot 10^5$	140	0.17 ± 0.11	39	0.22
0.985	33.08	2.48	0.12	1.24	0.006	0.20	$1.6 \cdot 10^5$	120	0.17 ± 0.11	44	0.24

must be subtracted from the mean heat flux, since the dynamo model makes the Boussinesq approximation in which the adiabatic gradient is already removed. Second, the laterally varying residual CMB heat flux $q - q_{ad}$ must be converted to non-dimensional co-density. Because we assume the dynamo is dominated by compositional convection, an appropriate non-dimensional scaling factor for the heat flux is $Q_c = \alpha\nu\ q_0/\beta k_c D\dot{\chi}$ (the subscript 'c' denotes 'core' as opposed to the scaling factor Q on the mantle side). The non-dimensional mean CMB co-density flux for the dynamo model then becomes

$$\frac{\partial C^*_0}{\partial r^*} = -q^*_{0c} = -Q_c\left(1 - \frac{q_{ad}}{q_0}\right) \tag{16}$$

and the non-dimensional amplitude of the CMB co-density heterogeneity for the dynamo models becomes

$$\delta\left(\frac{\partial C^*}{\partial r^*}\right) = -\delta q^*_c = -Q_c\frac{\delta q}{q_0}. \tag{17}$$

Table 2 summarizes the parameters used in the numerical dynamo simulations as well as some main results. In these models we have assumed that $q_{ad} = 2Q$ at $H^* = 1.24$, and furthermore, that a Rayleigh number $Ra = 1.2 \cdot 10^5$ corresponds to adiabatic CMB conditions $q_0 = q_{ad}$, so that $q^* = q^*_{0c} = 0$ at this Ra-value. Changes in q^*_{0c} relative to this reference state are then obtained from the dual pile curve for q^*_0 in Fig. 3a scaled according to (16). Likewise, changes in δq^*_c relative to the reference state $\delta q^*_{ad} = 2.69$ are obtained from the dual pile curve for δq^* in Fig. 3b scaled according to (17). Lastly, the relative changes in Ra are calculated assuming that Q_c remains constant in the outer core, so that Ra increases in proportion to q_0. We set $E = 6 \cdot 10^{-3}$, $Pr = 1$ and $Pm = 20$ in these cases.

Several reasons compel us to use dynamo models with these parameters. First, they lie within the parameter space identified by Christensen et al. (2010) as being Earth-like in terms of their magnetic field morphology. Second, they exhibit polarity reversals that are separated by stable polarity chrons in which the field is dominated by an axial dipole component. Third, the time-average reversal frequency in these dynamos changes systematically with the control parameters E and Ra, and with the boundary heterogeneity amplitude (Olson and Amit, 2014). Finally, the large E-value allows computing long time series, thereby registering enough reversals to construct meaningful statistics. There are of course drawbacks to our approach, perhaps the gravest being that these dynamos are very far from Earth-like status in terms of some individual control parameters, in particular, E and Pm. For this reason, we choose to focus attention on their qualitative behavior: Whether they reverse at all as well as the conditions under which they reverse frequently. In addition, we also include a couple of dynamo cases at $E = 1 \cdot 10^{-3}$ that show qualitative agreement.

Fig. 5 shows maps of the radial magnetic field on the outer boundary in the piles dynamos. Time-average maps were constructed by considering $+B_r$ during normal polarities and $-B_r$ during reversed polarities. Low H^* non-reversing dynamos yield radial field morphology with a clear signature of the CMB heat flux heterogeneity, in particular on time-average. This is evident by the two intense flux patches at each hemisphere in Fig. 5b that appear at about the same longitudes as the positive heat flux anomalies in the dual pile pattern (Fig. 4a). Although at a snapshot the correlation with the CMB heat flux pattern may be substantially inferior, there is a statistical preference for these intense flux patches to be aligned with the mantle heterogeneity (Olson and Christensen, 2002). Note that in the snapshot shown here (Fig. 5a) the equatorial symmetry and the order 2 dominance are preserved, although the patches are somewhat shifted in longitude with respect to the CMB heat flux pattern. Increasing Ra and H^* gives reversing dynamos with smaller scale more time-dependent fields (Fig. 5c) in which the mantle signature is less evident, probably requiring longer simulation times for statistical convergence. Nevertheless, the order 2 signature can still be identified in the time-average map of the larger Ra and H^* dual pile dynamo (Fig. 5d). Likewise, an order 1 signature characterizes the single pile dynamo (Fig. 5f), although it is surprisingly shifted by about 180° from the corresponding positive anomaly in the CMB heat flux pattern (Fig. 4b) due to strong westward drift driven by this particular boundary condition.

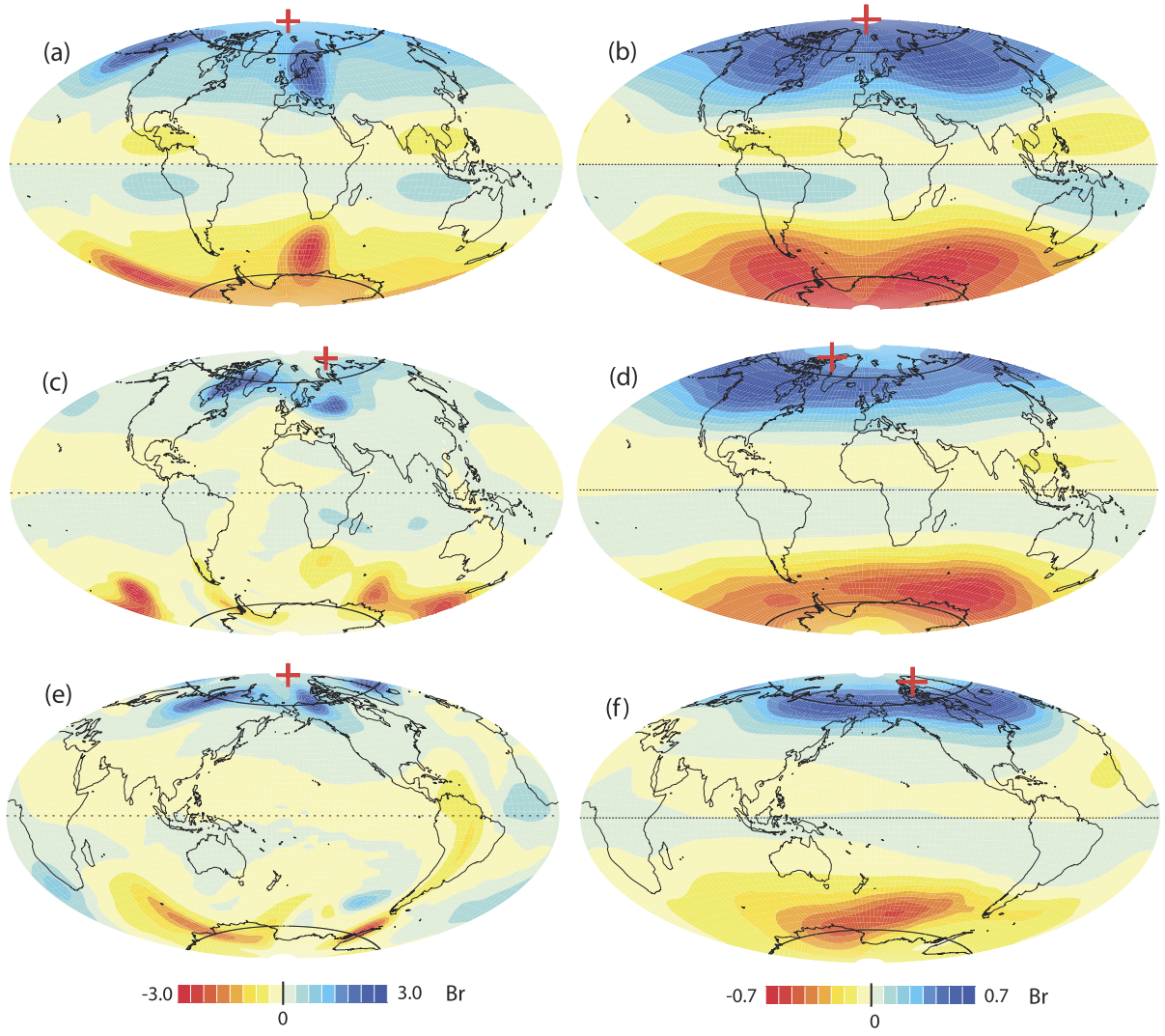

Fig. 5. Snapshot and time-average maps of the radial magnetic field on the CMB from the piles dynamos. Left column are snapshots, right column are time-averages. The radial magnetic field is given in non-dimensional (Elsasser number) units. Red crosses indicate geomagnetic dipole axis positions. Black lines denote the latitudes of the tangent cylinder. (a, b) Dual piles non-reversing dynamo with $H^*=1$ and $Ra=0.9\cdot 10^5$; (c, d) Dual piles reversing dynamo with $H^*=1.28$ and $Ra=1.3\cdot 10^5$; (e, f) Single pile reversing dynamo with $H^*=0.96$ and $Ra=1.2\cdot 10^5$. Note that the dual pile dynamos are centered at 0° longitude, whereas the single pile dynamo is centered at 180° longitude. (For interpretation of the references to color in this figure legend, the reader is referred to the web version of this article.)

Fig. 6 illustrates the dependence of the reversal frequency on the pile height as well as the irregularity of the chron durations. Pile dynamos with low H^* values exhibit very small dipole tilt oscillations (Fig. 6a), i.e. no apparent tendency to reverse. This state corresponds to superchron conditions in our models. Increasing H^* gives chaotic aperiodic reversals with strongly variable and irregular chron durations (Fig. 6b). A further increase in H^* leads to a stochastic hyper-reversing dynamo (Fig. 6c).

Fig. 7 shows the non-dimensional reversal frequency $N^*=N/\tau_d$ as functions of H^* and q_0^* for the first set of dual pile dynamos (Table 2, top). The error bars correspond to $\sqrt{N}/\tau_d$, consistent with Poisson distribution (Lhuillier et al., 2013). Reversal onset occurs near $H^*=1.2$ and $q_0^*=1.9$, and the reversal frequency increases approximately linearly beyond onset. The present-day (0–5 Ma) reversal rate of about 4 per million years corresponds to $N^*\simeq 0.2$, assuming $\tau_d=50$ kyr. By extrapolation, $N^*=0.2$ occurs near $H^*=1.35$ and $q_0^*=2.55$ in Figs. 7a and b, respectively. Accordingly, there is a fairly small window separating the pile height that would produce magnetic superchrons and the pile height that would produce frequent, and even hyper-frequent reversals. The associated increase in CMB heat flux is also relatively moderate, and amounts to a change of only ∼35% between these two dynamo states. The parameter ω_{sh} in Table 2 is the Sherman statistic for each reversal sequence. Random reversal sequences produce $\omega_{sh}\simeq 1/e$, whereas periodic and clustered reversal sequences have larger and smaller ω_{sh}-values, respectively (Olson et al., 2014).

To test these results, we also ran dual pile dynamos at $E=1\cdot 10^{-3}$ and larger Ra with the CMB heterogeneity parameters listed in the second set in Table 2 (middle). These dynamos have substantially greater flow velocities (magnetic Reynolds numbers above 400, as opposed to ∼150 for the first set cases) as well as smaller length scales, requiring substantially more numerical resolution and hence far longer running times, so that their reversal statistics are too meager to quantify reliably. Nevertheless, the results are qualitatively consistent with those of the first set and Fig. 7 in that increasing pile height transitions the dynamo from non-reversing to reversing behavior.

We have made a parallel series of calculations for single pile dynamos at $E=6\cdot 10^{-3}$ (for control parameters and summary results see the third set in Table 2 bottom). Fig. 8 shows the variation in non-dimensional reversal frequency vs. non-dimensional pile height and non-dimensional mean CMB heat flux for these cases. Note that the Rayleigh number for reversal onset in the single pile

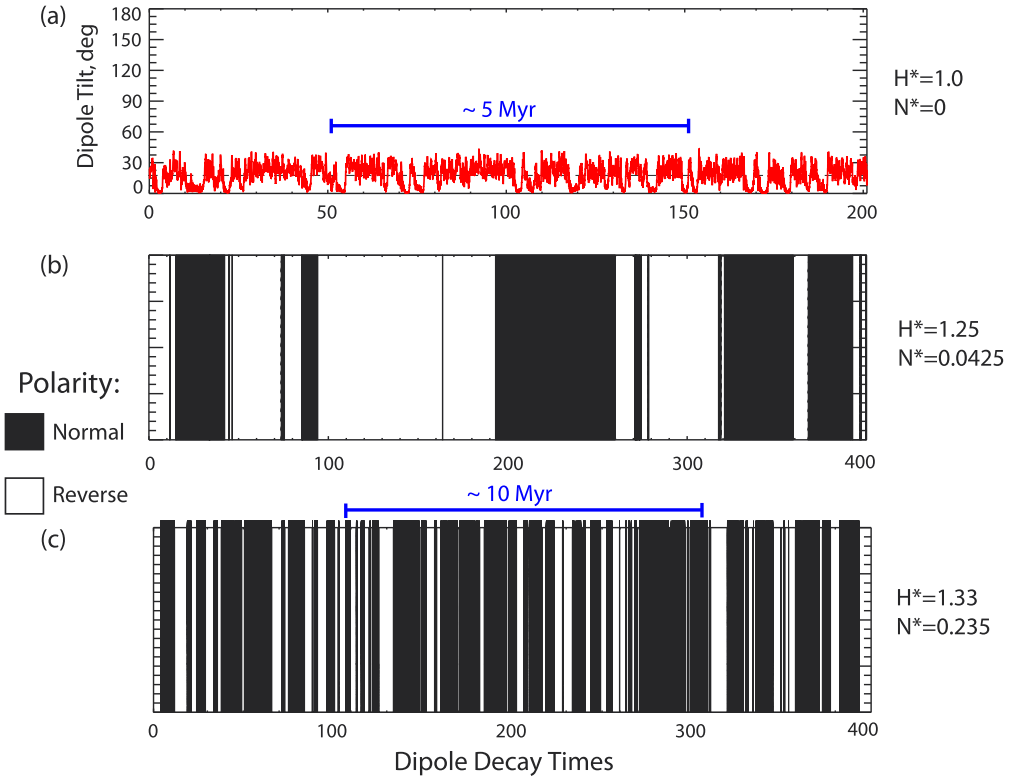

Fig. 6. Magnetic polarity timeseries in the dual pile dynamos with increasing H^*. Time is given in units of dipole decay time. (a) Dipole tilt timeseries (red) and its average (dashed black) in a non-reversing dynamo; (b, c) Polarity records for reversing dynamos. (For interpretation of the references to color in this figure legend, the reader is referred to the web version of this article.)

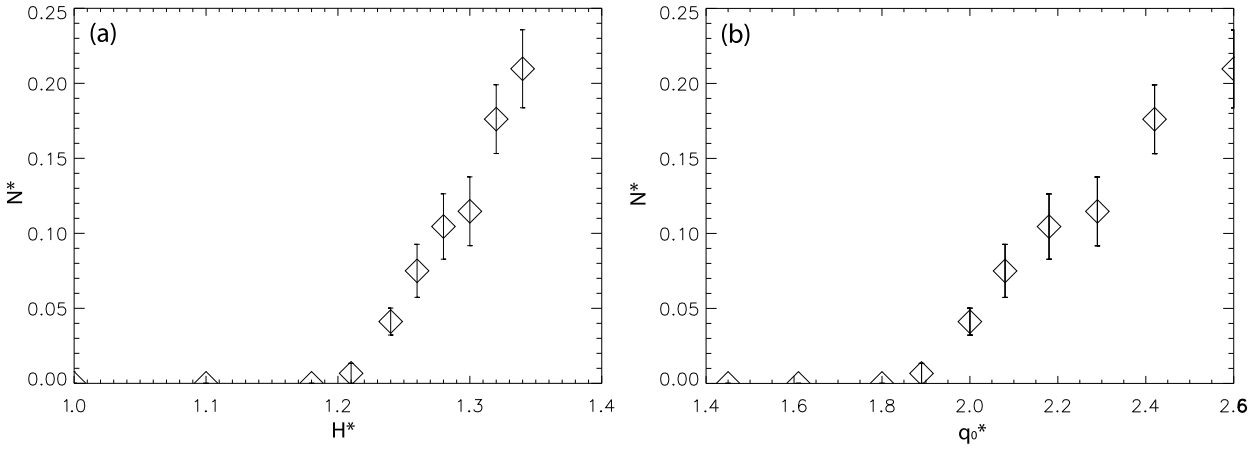

Fig. 7. Non-dimensional reversal frequency vs. non-dimensional piles height (a) and vs. non-dimensional mean CMB heat flux (b) in the set of dual pile (rotated Y_2^0) dynamo models.

dynamos in Table 2 bottom differs somewhat from the Rayleigh number for reversal onset in the dual pile dynamos in Table 2 top, and beyond onset their reversal frequencies differ somewhat. Even so, in qualitative terms the same behavior is found for these single pile cases as for the dual piles cases in Fig. 7. Specifically, the non-reversing state transitions to a reversing state at some critical value of H^* (or alternatively, q_0^*) and beyond this onset the rate of reversals increases rapidly, especially in terms of H^*. For both single and dual pile configurations the reversal frequency increases nearly linearly with H^*, but in terms of mean heat flux reversal frequency increases like $\sqrt{q_0^*}$. These trends are consistent with the non-linear relationship between q_0^* and H^* shown in Fig. 3a. In summary, the implications of pile growth and collapse are practically the same regardless of whether one pile or two piles are involved.

4. Discussion

Clearly our D″ pile model is very simplified. It is probable that complex dynamical scenarios in the lowermost mantle yield much more complex CMB heat flux patterns (e.g. Lay et al., 2008). For example, post-perovskite phase transition may cause spread piles with sharp edges and regions of enhanced CMB heat flux (Nakagawa and Tackley, 2011), thus distorting the idealized linear mapping between seismic and thermal anomalies at the D″ layer (Nakagawa and Tackley, 2008). Accounting for post-perovskite in the construction of CMB heat flux models may affect the morphology of persistent dynamo features (Amit and Choblet, 2009). Obtaining a more realistic CMB heat flux pattern from a refined D″ pile model is worth-while, but it is beyond the scope of this study.

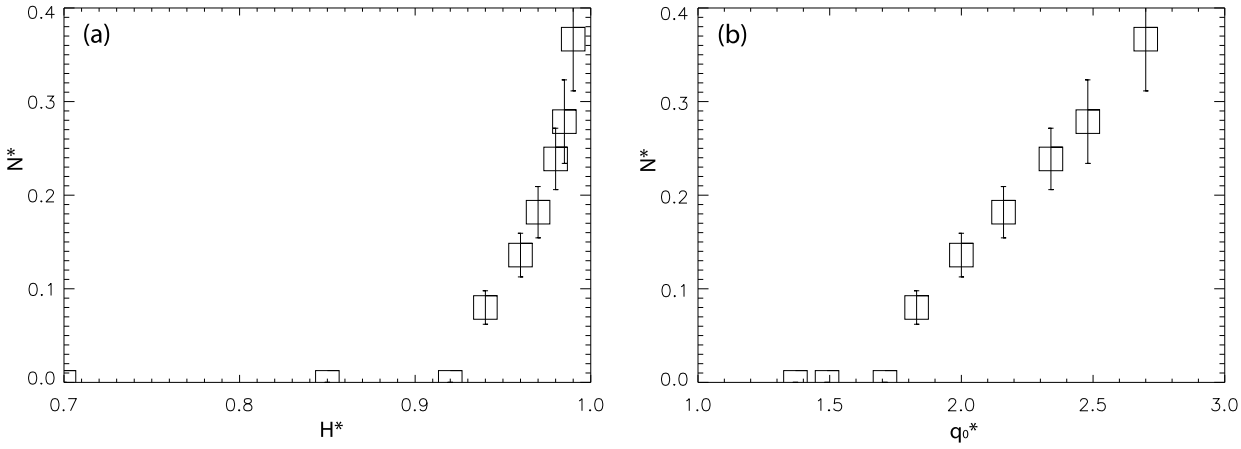

Fig. 8. As in Fig. 7 for the set of single pile (rotated Y_1^0) dynamo models.

Although our D″ pile model is highly simplified and the reversing numerical dynamo models are very large-scale, some useful insights may be drawn. Assuming that the D″ layer volume and the temperature difference across the D″ are both conserved in time, we have shown theoretically that the mean CMB heat flux rapidly increases as D″ chemical piles grow (Fig. 3a). The amplitude of the CMB heat flux heterogeneity δq^* also increases with growing piles (Fig. 3b). Reversals in numerical dynamo models with heterogeneous CMB heat flux are more frequent when the mean is increased, and in the tomographic case also when the amplitude of the lateral heterogeneity is increased (Olson et al., 2010; Heimpel and Evans, 2013; Olson and Amit, 2014). It was not clear a priori whether the CMB heat flux pattern of the dual pile structure would enhance or suppress reversals, especially since it contains a significant zonal component that may work either way (Olson and Amit, 2014). Our numerical dynamo models show that these two effects work in unison to increase reversal frequency with growing piles.

The longevity of the dual pile structure in the lower mantle remains controversial. Volcanic hotspot reconstructions (Torsvik et al., 2006) point to the existence of two superplumes far back into the Paleozoic, whereas mantle global circulation models predict a single superplume during Pangaea assembly prior to 330 Ma (Zhang et al., 2010) and superchron conditions in the core during the transition (Olson et al., 2013). Our D″ model predicts that geomagnetic reversals are stimulated by piles growth in either configuration.

Most tomographic heat flux patterns are dominated by the Y_2^2 spherical harmonic. The rotated Y_2^0 pattern used in our study also contains a significant Y_2^2 component, but in addition a $+Y_2^0$ contribution appears (Fig. 4a). This polar cooling may have a substantial effect on reversal frequency. Previous studies found that polar cooling stabilizes the dynamo and may yield superchrons (Glatzmaier et al., 1999; Kutzner and Christensen, 2004). Olson and Amit (2014) argued that close to the onset of reversals polar cooling indeed inhibits reversals, but farther from the onset the opposite effect occurs and polar cooling increases reversal frequency. These special effects of zonal heterogeneity in the CMB heat flux pattern motivate further inspection of the rotated Y_2^0 pattern and its impact on reversal frequency.

An exact quantitative comparison between our results to those obtained by tomographic dynamos (e.g. Olson and Amit, 2014) is difficult, because in previous studies the mean CMB heat flux and the heterogeneity amplitude are two independent parameters, whereas in our D″ pile model both quantities are controlled by the piles height. Based on the linear fits obtained by Olson and Amit (2014) with tomographic patterns, an increase of ∼10% in the mean CMB heat flux (corresponding to an increase of ∼5% in the local Rossby number) with an arbitrary reference reversal frequency of $N^* = 0.1$ would give an increase of ∼25% in the reversal frequency. In contrast, with our D″ pile model the same increase of ∼10% in the mean CMB heat flux with a reference $N^* = 0.1$ results in an increase of ∼70% in the reversal frequency (Fig. 7b). It is likely that the reason for this much larger increase in reversal frequency with our D″ pile model is that the heterogeneity amplitude increases together with the mean CMB heat flux (Fig. 3).

Our results are qualitatively consistent with predictions from previous dynamo reversal studies (Kutzner and Christensen, 2004; Olson et al., 2010; Driscoll and Olson, 2011; Olson and Amit, 2014). Intense outer core convection, high CMB heat flux and fully developed lower mantle piles correspond to times with frequent polarity reversals, whereas superchrons correspond to times with weaker core convection, lower CMB heat flux and reduced piles height. In particular, the onset and termination of the CNS and KRS superchrons (Fig. 1) may mark piles partial collapse and growth stages, respectively. The modulation of piles height and subsequent CMB heat flux needed to explain the observed variability in paleomagnetic reversal frequency is modest; The increase in piles height that is needed to go from non-reversing superchron conditions $N^* = 0$ during the CNS to present-day rapidly reversing conditions of $N^* = 0.2$ is ∼13%, and the corresponding increase in mean CMB heat flux is ∼35%. Such changes are only slightly larger than those found in mantle general circulation models (Zhang and Zhong, 2011; Nakagawa and Tackley, 2013; Olson et al., 2013), although the fluctuations in CMB heat flux predicted by the latter models are in many cases not closely in phase with the reversal frequency variations during this time interval.

There is independent observational support for Cenozoic superplume growth, based on the uplift history of the African continent and the origin of the African Superswell on the nearby ocean floor (Nyblade and Robinson, 1994). The timing of the uplift of Africa (Bond, 1978) coincides with the trend of increasing geomagnetic reversal frequency in the Cenozoic C-sequence, as our model predicts. Geodynamic considerations (Lithgow-Bertelloni and Silver, 1998) indicate that the African Superswell is supported by a mantle upwelling, and mantle reconstructions indicate that this upwelling has strengthened over the past 80 Myr through growth of the lower mantle African superplume (Conrad and Gurnis, 2003). It has been proposed that Cenozoic tectonic uplift has aridified East Africa, driving climate change and forcing early hominid evolution in that region (Sepulchre et al., 2006). Likewise, it has been suggested that superplume growth terminated the KRS, leading to formation of the Siberian Traps and contributing to the Permian mass extinction (Courtillot and Olson, 2007). Through such inter-

actions, superplumes in the deep mantle may impact the climate system as well as the geodynamo.

Acknowledgements

P.O. was supported by Frontiers in Earth System Dynamics grant EAR-1135382 from the National Science Foundation. We thank two anonymous reviewers for their constructive reviews. We are grateful to U. Christensen for helpful discussions.

References

Amit, H., Choblet, G., 2009. Mantle-driven geodynamo features – effects of post-perovskite phase transition. Earth Planets Space 61, 1255–1268.
Aubert, J., Labrosse, S., Poitou, C., 2009. Modelling the paleo-evolution of the geodynamo. Geophys. J. Int. 179, 1414–1428.
Biggin, A.J., Steinberger, B., Aubert, J., Suttie, N., Holme, R., Torsvik, T.H., van der Meer, D.G., van Hinsbergen, D.J.J., 2012. Possible links between long-term geomagnetic variations and whole-mantle convection processes. Nat. Geosci. 5, 526–533.
Bond, G., 1978. Evidence for late Tertiary uplift of Africa relative to North America, South America, Australia and Europe. J. Geol. 86, 47–65.
Braginsky, S.I., Roberts, P.H., 1995. Equations governing convection in Earth's core and the geodynamo. Geophys. Astrophys. Fluid Dyn. 79, 1–97.
Bull, A., McNamara, A., Ritsema, J., 2009. Synthetic tomography of plume clusters and thermochemical piles. Earth Planet. Sci. Lett. 278, 152–162.
Burke, K., 2011. Plate tectonics, the Wilson cycle, and mantle plumes: geodynamics from the top. Annu. Rev. Earth Planet. Sci. 39, 1–29.
Burke, K., Steinberger, B., Torsvik, T.H., Smethhurst, M.A., 2008. Plume generation zones at the margins of large low shear velocity provinces on the core–mantle boundary. Earth Planet. Sci. Lett. 265, 49–60.
Christensen, U., Aubert, J., 2006. Scaling properties of convection-driven dynamos in rotating spherical shells and application to planetary magnetic fields. Geophys. J. Int. 166, 97–114.
Christensen, U., Aubert, J., Hulot, G., 2010. Conditions for Earth-like geodynamo models. Earth Planet. Sci. Lett. 296, 487–496.
Christensen, U., Wicht, J., 2007. Numerical dynamo simulations. In: Olson, P. (Ed.), Treatise on Geophysics, vol. 8. Elsevier Science.
Conrad, C., Gurnis, M., 2003. Seismic tomography, surface uplift, and the breakup of Gondwanaland: integrating mantle convection backwards in time. Geochem. Geophys. Geosyst. 4. http://dx.doi.org/10.1029/2001GC000299.
Courtillot, V., Olson, P., 2007. Mantle plumes link magnetic superchrons to Phanerozoic mass depletion events. Earth Planet. Sci. Lett. 260, 495–504.
Driscoll, P.E., Olson, P.L., 2009a. Effects of buoyancy and rotation on the polarity reversal frequency of gravitationally-driven numerical dynamos. Geophys. J. Int. 178, 1337–1350.
Driscoll, P.E., Olson, P.L., 2009b. Polarity reversals in geodynamo models with core evolution. Earth Planet. Sci. Lett. 282 (1–4), 24–33.
Driscoll, P.E., Olson, P.L., 2011. Superchron cycles driven by variable core heat flow. Geophys. Res. Lett. 38 (9), L09304.
Dziewonski, A.M., Lekic, V., Romanowicz, B.A., 2010. Mantle anchor structure: an argument for bottom up tectonics. Earth Planet. Sci. Lett. 299, 69–79.
Garnero, E., McNamara, A., 2008. Structure and dynamics of Earth's lower mantle. Science 320, 626–628.
Glatzmaier, G., Coe, R., Hongre, L., Roberts, P., 1999. The role of the Earth's mantle in controlling the frequency of geomagnetic reversals. Nature 401, 885–890.
Gradstein, F., Ogg, J., Schmitz, M., Ogg, G., 2012. The Geologic Time Scale 2012. Elsevier Science, Amsterdam.
Heimpel, M.H., Evans, M.E., 2013. Testing the geomagnetic dipole and reversing dynamo models over Earth's cooling history. Phys. Earth Planet. Inter. 224, 124–131.
Kutzner, C., Christensen, U.R., 2004. Simulated geomagnetic reversals and preferred virtual geomagnetic pole paths. Geophys. J. Int. 157, 1105–1118.
Lay, T., Herlund, J., Buffett, B.A., 2008. Core–mantle boundary heat flow. Nat. Geosci. 1, 25–32.
Lhuillier, F., Hulot, G., Gallet, Y., 2013. Statistical properties of reversals and chrons in numerical dynamos and implications for the geodynamo. Phys. Earth Planet. Inter. 220, 19–36.
Lithgow-Bertelloni, C., Richards, M.A., 1998. Dynamics of Cenozoic and mesozoic plate motion. Rev. Geophys. 36, 27–78.
Lithgow-Bertelloni, C., Silver, P.G., 1998. Dynamic topography, plate driving forces and the African superswell. Nature 395, 269–272.
Masters, G., Laske, G., Bolton, H., Dziewonski, A., 2000. The relative behavior of shear velocity, bulk sound velocity, and compressional velocity in the mantle: implications for chemical and thermal structure. In: Karato, S., Forte, A., Liebermann, R., Masters, G., Stixrude, L. (Eds.), Earths Deep Interior. In: AGU Monograph, vol. 117. American Geophysical Union, Washington, DC.
McNamara, A., Zhong, S., 2005. Thermochemical structures beneath Africa and the Pacific Ocean. Nature 437, 1136–1139.
Merrill, R.T., McElhinny, M.W., McFadden, P.L., 1998. The Magnetic Field of the Earth: Paleomagnetism, the Core, and the Deep Mantle. Academic Press, San Diego, California, USA.
Nakagawa, T., Tackley, P.J., 2008. Lateral variations in CMB heat flux and deep mantle seismic velocity caused by a thermal-chemical-phase boundary layer in 3D spherical convection. Earth Planet. Sci. Lett. 271, 348–358.
Nakagawa, T., Tackley, P.J., 2011. Effects of low-viscosity post-perovskite on thermo-chemical mantle convection in a 3-D spherical shell. Geophys. Res. Lett. 38, L04309.
Nakagawa, T., Tackley, P.J., 2013. Implications of high core thermal conductivity on Earth's coupled mantle and core evolution. Geophys. Res. Lett. 40, 2652–2656.
Nyblade, A.A., Robinson, S.W., 1994. The African superswell. Geophys. Res. Lett. 21. http://dx.doi.org/10.1029/94GL00631.
Olson, P., 2007. Gravitational dynamos and the low frequency geomagnetic secular variation. Proc. Natl. Acad. Sci. 104, 20159–20166.
Olson, P., Amit, H., 2014. Magnetic reversal frequency scaling in dynamos with thermochemical convection. Phys. Earth Planet. Inter. 229, 122–133.
Olson, P., Christensen, U., 2002. The time averaged magnetic field in numerical dynamos with nonuniform boundary heat flow. Geophys. J. Int. 151, 809–823.
Olson, P., Christensen, U., 2006. Dipole moment scaling for convection-driven planetary dynamos. Earth Planet. Sci. Lett. 250, 561–571.
Olson, P., Coe, R.S., Driscoll, P.E., Glatzmaier, G.A., Roberts, P.H., 2010. Geodynamo reversal frequency and heterogeneous core–mantle boundary heat flow. Phys. Earth Planet. Inter. 180, 66–79.
Olson, P., Deguen, R., Hinnov, L.A., Zhong, S., 2013. Controls on geomagnetic reversals and core evolution by mantle convection in the Phanerozoic. Phys. Earth Planet. Inter. 214, 87–103.
Olson, P., Hinnov, L.A., Driscoll, P.E., 2014. Nonrandom geomagnetic reversal times and geodynamo evolution. Earth Planet. Sci. Lett. 388, 9–17.
Pétrélis, F., Besse, J., Valet, J.P., 2011. Plate tectonics may control geomagnetic reversal frequency. Geophys. Res. Lett. 38, L19303.
Pétrélis, F., Fauve, S., Dormy, E., Valet, J.P., 2009. Simple mechanism for reversals of Earth's magnetic field. Phys. Rev. Lett. 102, 144503.
Romanowicz, B., Gung, Y., 2002. Superplumes from the core–mantle boundary to the lithosphere: implications for heat flux. Science 296, 513–516.
Ryan, D.A., Sarson, G.R., 2007. Are geomagnetic field reversals controlled by turbulence within the Earth's core? Geophys. Res. Lett. 34, L02307. http://dx.doi.org/10.1029/2006GL028291.
Schubert, G., Masters, G., Olson, P., Tackley, P., 2004. Superplumes or plume clusters? Phys. Earth Planet. Inter. 146, 147–162.
Sepulchre, P., Ramstein, G., Fluteau, F., Schuster, M., Tiercelin, J.-J., Brunet, M., 2006. Tectonic uplift and Eastern Africa aridification. Science 313, 1419–1423.
Tackley, P., 2002. The strong heterogeneity caused by deep mantle layering. Geochem. Geophys. Geosyst. 3. http://dx.doi.org/10.1029/2001GC000167.
Tan, E., Gurnis, M., 2007. Compressible thermochemical convection and application to lower mantle structures. J. Geophys. Res. 112. http://dx.doi.org/10.1029/2006JB004505.
Torsvik, T.H., Burke, K., Steinberger, B., Webb, S.J., Ashwel, L.D., 2010. Diamonds sampled by plumes from the core–mantle boundary. Nature 466, 352–355.
Torsvik, T.H., Smethhurst, M.A., Burke, K., Steinberger, B., 2006. Large igneous provinces generated from the margins of the large low-velocity provinces in the deep mantle. Geophys. J. Int. 167, 1447–1460.
Wicht, J., Stellmach, S., Harder, H., 2009. Numerical models of the geodynamo: from fundamental Cartesian models to 3D simulations of field reversals. In: Glassmeier, H., Soffel, H., Negendank, J. (Eds.), Geomagnetic Field Variations – Space–time Structure, Processes, and Effects on System Earth. Springer, Berlin.
Zhang, N., Zhong, S., 2011. Heat fluxes at the Earth's surface and core–mantle boundary since Pangea formation and their implications for the geomagnetic superchrons. Earth Planet. Sci. Lett. 306, 205–216.
Zhang, N., Zhong, S.J., Leng, W., Li, Z.X., 2010. A model for the evolution of the Earth's mantle structure since the early Paleozoic. J. Geophys. Res. 115, B06401.